

THE EXAMPLE MEASUREMENTS
COSMICWATCH
THE DESKTOP MUON DETECTOR (v3X)

Contacts:

Prof. Spencer N. Axani (saxani@udel.edu)

Masooma Sarfraz (masoomas@udel.edu)

Miles Garcia (milesg@udel.edu)

Katarzyna Frankiewicz (katarzyna.frankiewicz@gmail.com)

Prof. Janet M. Conrad (conradg@mit.edu)

August 20, 2025

© 2025 University of Delaware, Professor Spencer N.G. Axani
Commercial use of this work is prohibited without explicit written permission from the copyright holder.

The original author retains exclusive rights to sell or commercially distribute this device.
This work is licensed under the Creative Commons Attribution-NonCommercial 4.0 International License.

To view a copy of this license, visit <https://creativecommons.org/licenses/by-nc/4.0/>

Contents

1 DOCUMENT OVERVIEW	4
2 TESTED MEASUREMENTS	7
2.1 A full-sky cosmic-ray muon measurement	8
2.2 Cosmic-ray muon angular dependence	10
2.3 Muon rate measurement while flying to the South Pole	11
2.4 Latitude correction to the cosmic-ray muons	13
2.5 High-altitude balloon flight	14
2.6 Cosmic-ray muon velocity	15
2.7 Cosmic-ray muon attenuation in a Subway station	16
2.8 Electromagnetic component of cosmic-ray showers	17
2.9 Reducing radioactive backgrounds	19
2.10 Correlation between the cosmic-ray muon rate and atmospheric pressure	20
2.11 A true random number generator?	22
2.12 Gamma-ray spectroscopy	25
2.13 Measuring the cosmic-ray muon rate in an airplane at 33,000 ft	26
2.14 High altitude balloon measurement at 107,000 ft	27
2.15 Rate measurement 1 km underground at Super-Kamiokande	29
2.16 Portable trigger system for an accelerator beamline	31
3 UNTESTED MEASUREMENTS FOR THE ADVENTUROUS	32
3.1 Muon Rate Underwater	33
3.2 Muon lifetime	34
3.3 Solar flares and the Forbush decrease	35
3.4 Measuring the air shower size	36
4 CONCLUSION	38

Chapter 1

DOCUMENT OVERVIEW

The CosmicWatch Detector v3X is a compact, self-contained, inexpensive (100\$), low-power (0.5 W), particle detector that uses a plastic scintillator and silicon photomultiplier to explore particle, nuclear, astro-, and geophysics. Through these detectors we can explore a wide range of phenomena, including muon energy loss in materials, special relativity, radioactive decay, cosmic ray shower composition, and much more. The detectors support standalone data logging to microSD or live USB streaming, offers coincidence mode for background suppression, and logs rich event metadata (e.g. timestamp, ADC value, temperature, pressure, acceleration). Fully open-source with detailed build instructions and provided Python analysis scripts, v3X will be useful for education, outreach, citizen science, and more advanced cosmic-ray studies.

This instruction manual provides a comprehensive exploration of the CosmicWatch Desktop Muon Detectors v3X. It starts by describing the sources of ionizing radiation that we need to consider for the remainder of the document. After that, we'll work through how each of these forms of radiation interact with materials and how the detectors measure their interaction. We'll then shift to details specific to the detectors, discussing the technology employed and provide instructions on how to build a detector yourself. The last few chapters of the document illustrates various physical phenomena discussed in earlier chapters through measurements conducted specifically with the detectors. As students generate new study ideas using this detector and analyze fresh data, these concluding chapters are envisioned to undergo continuous updates.

All material for v3X can be found in the GitHub repository located here:

<https://github.com/spenceraxani/CosmicWatch-Desktop-Muon-Detector-v3X>

Version v3X represents a significant advancement over the previous v2 detector. In addition to the significant improvements in the analog electronics, high-frequency PCB design, and component optimization, v3X delivers orders-of-magnitude enhancements across several performance metrics and also introduces new functionality, as illustrated in Fig. ??.

CosmicWatch v2	Specification	CosmicWatch v3X
ATmega328P	Processor	Cortex-M0+
Single Core	Number of cores	Dual Core
16 MHz	Clock frequency	133 MHz
32 KB	Flash memory	2 MB
2 KB	RAM	264 KB
0.27 W	Power consumption	0.5 W
<8-bit	ADC resolution	12-bit
15 Hz	Maximum event rate	700 Hz
0.5 mV RMS	Noise level	0.1 mV RMS
Yes	microSD Card	Yes
Yes (w/o SD card)	OLED readout	Yes
Yes	Temperature sensor	Yes
No	Pressure sensor	Yes
No	Accelerometer & gyroscope	Yes
No	Buzzer	Yes
25 cm ²	Effective area	25 cm ²
50 ms	dead time per event	400 μs
106 g	Dry weight	110 g
36 mm ²	Photocathode area	36 mm ²
No	Citizen science support	Yes
12 mV	Min. trigger threshold	4 mV
4.5×10^{-4} Hz	Accidental coincidence rate	6.0×10^{-6} Hz
\$100	Approximate cost	\$100

Table 1.1: Specification comparison between CosmicWatch v2 and v3X detectors. Bold entries indicate the specification with superior performance.

Many documents have played a crucial role in compiling this information. A great and valuable reference, is the Particle Data Group’s (PDG) summary on cosmic rays [1] and energy loss in matter [2]. MIT Prof. Bruno Rossi’s textbook, *Cosmic Rays* from 1964 [3], is a great entry-level resource, providing an early account of cosmic-ray physics investigations. It not only offers insightful reading but also allows readers to replicate many of the experiments conducted for the first time using the CosmicWatch detectors.

For a more contemporary perspective with a focus on history, Prof. M. Friedlander’s book titled *A Thin Cosmic Rain* [4] is recommended. Dr. P. Grieder’s comprehensive textbook, *Cosmic Rays at Earth* [5], provides an in-depth overview of cosmic-ray physics and will be frequently referenced. For higher-energy cosmic-ray physics, Prof. T. Gaisser’s book (from the University of Delaware), *Cosmic Rays and Particle Physics* [6], proves to be extremely useful.

For a comprehensive understanding of energy loss in matter, *Techniques for Nuclear and Particle Physics* by W. Leo [7] stands out as one of the best resource for experimental particle physics. Additionally, Prof. C. Grupen’s textbook, *Particle Detectors* [8] and *Particle Detectors: Fundamentals and Applications* [9] by H. Kolanoski, are extremely highly recommended as a reference for describing detection methods in particle physics.

Components of this instructions manual has been lightly adapted from MIT’s Junior Lab

Manual, which was based off of Prof. Spencer Axani’s Masters Thesis, accessible directly at <https://arxiv.org/abs/1908.00146>. However, this is a new detector, specifically designed to increase the CosmicWatch’s physics, education, and industrial reach, as well as providing the backbone for a future citizen science project.

The original CosmicWatch project was significantly developed with co-collaborator Dr. Katarzyna Frankiewicz and Prof. Janet Conrad. The original project has had funding from the MIT Physics Department, the Wisconsin Particle Astrophysics Center (WiPAC), the National Science Foundation (NSF), and is now funded through the University of Delaware (UD).

We are excited to have the CosmicWatch detector incorporated into the Experimental Methods in Physics courses at UD. Developing this detector has been a passion, not just a hobby. We hope you enjoy it, and even consider building your own.

Chapter 2

TESTED MEASUREMENTS

You will design your own experiment for this laboratory class. The list below are some measurements that can be done at home, the lab, or office. Feel free to choose from this list or develop your own idea! Inspiration for new ideas may come from measurements described in Sec. ??.

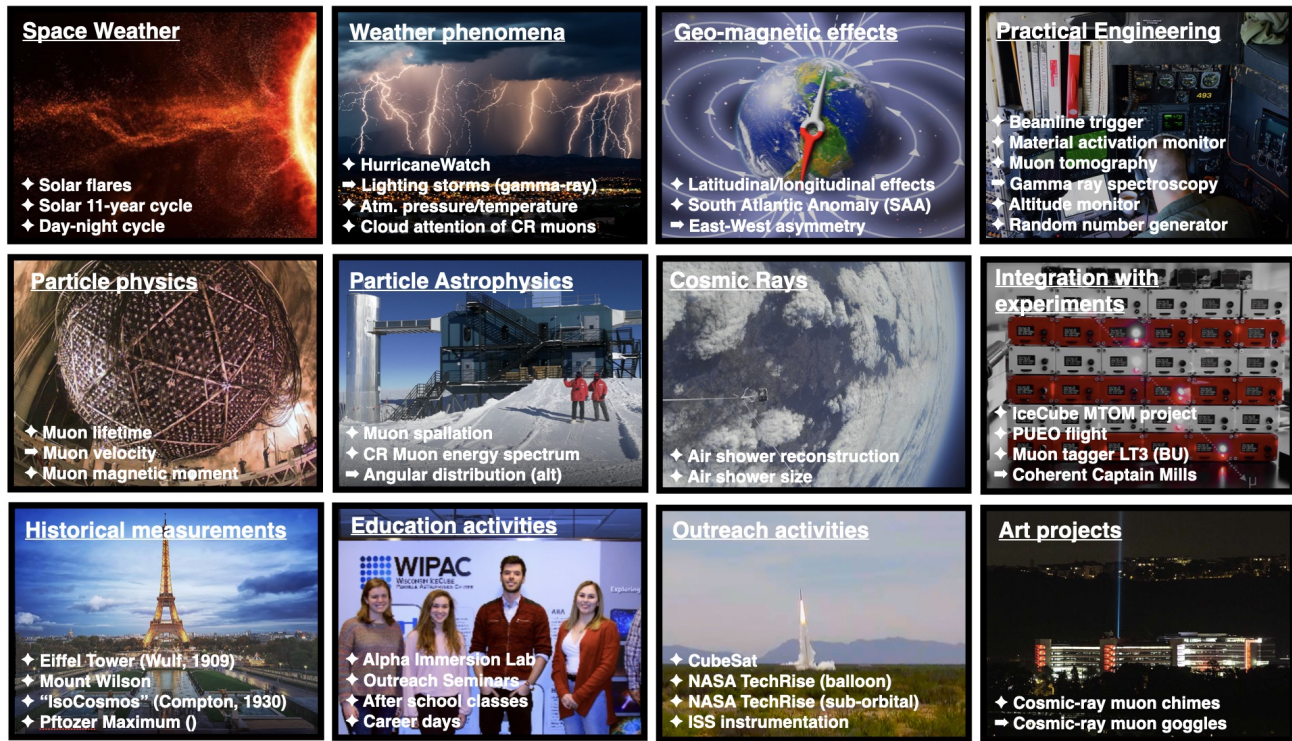


Figure 2.1: This figure gives you an overview of the scope of the muon detectors. Some of these measurements will be described below, other we are still working on.

2.1 A full-sky cosmic-ray muon measurement

Two v3X detectors were arranged in configuration (d), as shown in Fig. ??, in the basement of Sharp Lab to maximize the solid-angle acceptance to $\Omega \approx 2\pi \text{ sr}$. Data presented in Fig. ?? were recorded continuously to microSD cards over 26.9 h, yielding a total of $N_{\text{total}} = 2.35 \times 10^4$ events and $N_{\text{coin}} = 3.05 \times 10^4$ coincident events. These correspond to a total trigger rate of $R_{\text{total}} = 2.423 \pm 0.005 \text{ Hz}$ and a coincidence rate of $R_{\text{coin}} = 0.315 \pm 0.002 \text{ Hz}$, or $0.756 \pm 0.005 \text{ cm}^{-1}\text{s}^{-1}$. The total dead time during this measurement was 0.1% of the livetime, corresponding to an average dead time per event of $408 \mu\text{s}$.

The SiPM pulse-height spectrum (Fig. 2.2, left) exhibits the characteristic Landau-shaped “minimum ionizing particle (MIP) bump” produced by through-going muons in a thin absorber. The Landau energy-loss distribution can be approximated by the analytic Moyal distribution [?, 9]:

$$f(x; \mu, c) = \frac{1}{\sqrt{2\pi}c} \exp\left[-\frac{1}{2}(z + e^{-z})\right] \quad \text{with} \quad z = \frac{x - \mu}{c}, \quad (2.1)$$

where μ denotes the most probable value and c the width parameter. A fit over the range 13 mV to 40 mV yields $\mu \approx 21 \text{ mV}$, which corresponds to the $\sim 2 \text{ MeV}$ energy loss of a minimum-ionizing muon traversing the $\approx 1 \text{ cm}$ -thick plastic scintillator [?], and $c \approx 5 \text{ mV}$. This is only approximate, as the average trajectory of the muons through the scintillator will be slightly larger than 1 cm. Detector saturation appears near 180 mV, as denoted by the overflow bin. The relatively flat tail below 10 mV in the coincident-event distribution is attributed to corner-clipping muons, which graze the scintillator edge and deposit reduced energy.

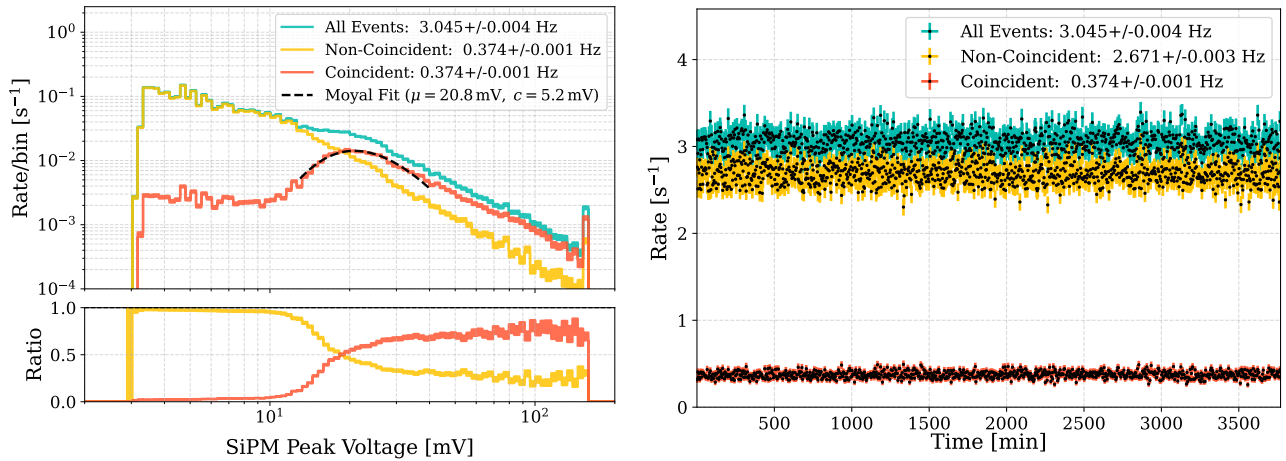


Figure 2.2: Left: the SiPM pulse-height spectra recorded by a set of detector in configuration (d). The coincident events begin dominating at SiPM pulse-heights greater than approximately 18 mV. Right: The measured detection rate of coincident and non-coincident events.

This demonstrates the ability to select muons using *coincidence mode* and shows how the SiPM pulse amplitude can be used to discriminate between muons and radiogenic backgrounds based

on energy deposition. The ratio plotted in the left subplot of Fig. 2.2 indicates that above approximately 18 mV, cosmic-ray muons dominate the spectrum.

The precise location of the MIP peak depends on the quality of the detector assembly: the efficiency of the optical coupling between the SiPM and scintillator, the scintillator surface finish, the reflectivity of any wrapping, and other factors that influence photon collection. It also shifts with the SiPM bias voltage, which is set by precision (0.1 %) resistors and directly determines the gain. Nevertheless, because the MIP peak occurs well above the trigger threshold (≈ 4 mV), even substantial variations in collection efficiency have minimal effect on muon detection efficiency; only corner-clipping events register near threshold. Overall count rates, however, are expected to show more significant detector-to-detector variations due to the steep rise of the non-coincident background near threshold.

Fig. 2.2 (right) displays the event rate versus time for the same dataset, comparing non-coincident and coincident counts. Each point represents a 240 s interval, with the rate calculated as the number of events divided by the effective live time (bin duration minus total dead time). These rate measurements enable searches for correlations with atmospheric variables—e.g., barometric pressure changes (Fig. 2.3 (left))—or transient phenomena such as solar flares. The detector also logs temperature (Fig. 2.3 [right]), allowing corrections for temperature-dependent gain shifts, although it currently isn't implemented.

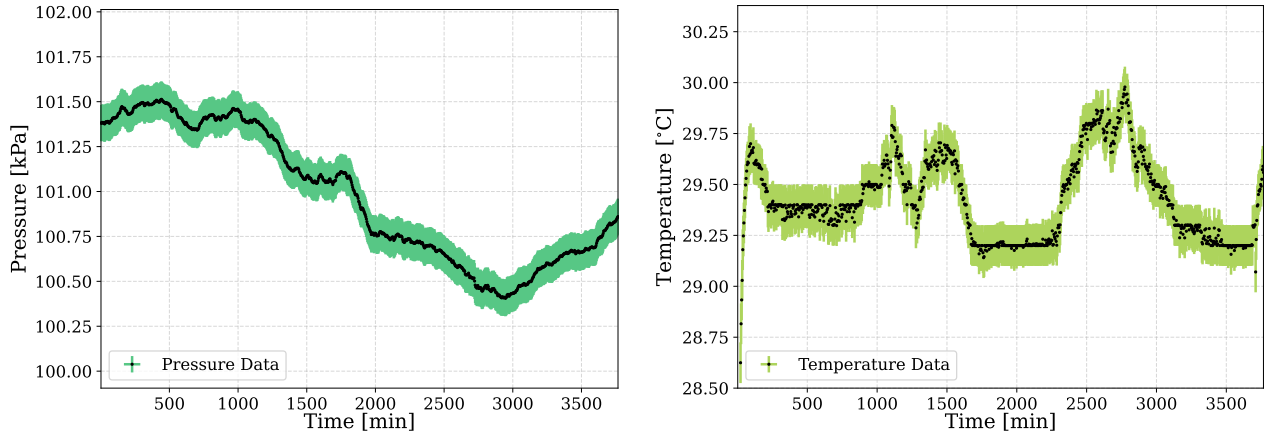


Figure 2.3: Left: Barometric pressure recorded by the onboard BMP280 sensor over time. Right: Temperature measured by the same sensor, used to monitor environmental conditions and correct for temperature dependent SiPM gain variations.

2.2 Cosmic-ray muon angular dependence

This measurement illustrates the cosmic-ray muon angular dependence measured near sea level. Two detectors were operated in coincidence mode and positioned side-by-side (configuration (a) in Fig. ??), with their scintillators separated by 50 mm inside identical aluminum enclosures. The detector angle θ was set by mounting both units on a 40 cm rectangular bar and leaning the bar against a vertical wall at a known height (see Fig. 2.4, right). Fig. 2.4 (left) shows the measured rate as a function of zenith angle. Each data point represents approximately 24 hours of data, and the rate uncertainties are purely statistical.

In this configuration, the detectors are oriented to sample muons within $\pm 20^\circ$ of the set angle. Several contributions to the measured rate are expected. First, the angular dependence of cosmic-ray muons at sea level follows a cosine-squared law, $I(\theta) \propto \cos^2\theta$, where $I(\theta)$ is the differential muon intensity as a function of zenith angle θ (with $\theta = 0^\circ$ corresponding to vertically downward-going muons) [?]. Second, there is an accidental coincidence rate

$$R_{\text{acc}} = 2 N_1 N_2 \tau, \quad (2.2)$$

where $N_1 = 3.3$ Hz and $N_2 = 2.9$ Hz are the individual detector trigger rates, and $\tau = 2.3 \mu\text{s}$ is the coincidence window. Finally, extensive air showers produce muon bundles, multiple muons arriving simultaneously from a single primary cosmic-ray interaction, which can trigger both detectors, resulting in a higher coincidence rate at all angles. Figure 2.4 overlays the expected $\cos^2\theta$ dependence and the flat accidental background rate, together with the remaining offset attributed to the air-shower contribution.

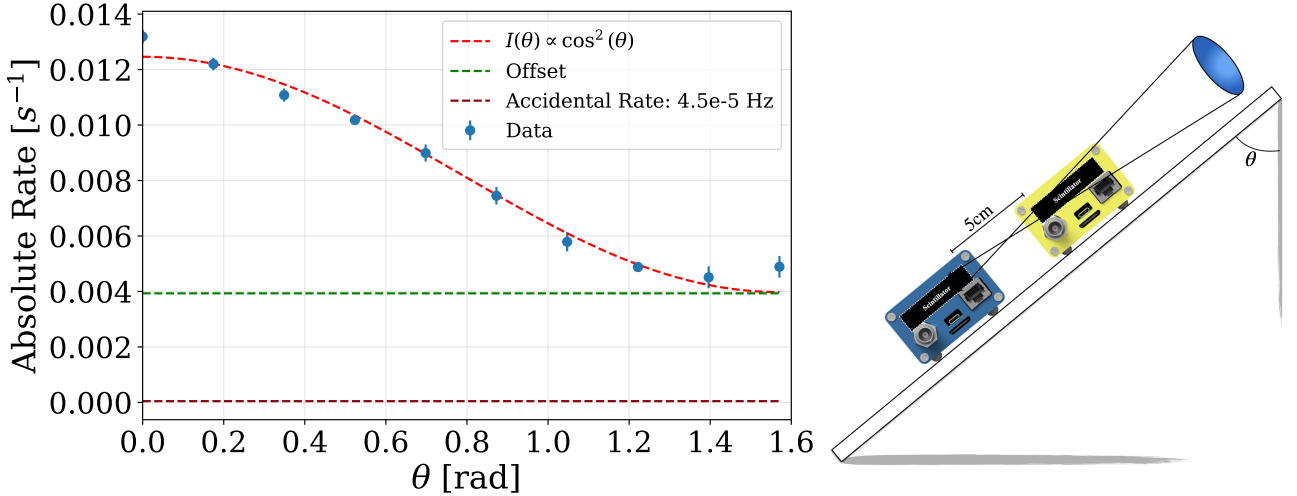


Figure 2.4: Left: The measured cosmic-ray muon angular distribution along with the fitted components to the data. Right: An illustration of the measurement configuration.

A slight increase in rate at $\theta = \pi/2$ is attributed to this configuration accepting muons from both upward and downward directions, whereas all other orientations record only downward-going muons. Therefore, the single-muon contribution at $\theta = \pi/2$ should, in principle, be halved.



DEPLOYMENT TO THE SOUTH POLE

AIRCRAFT: C-130 HERCULES

LOCATION: WILLY'S FIELD MCMURDO

Figure 2.5: Leaving McMurdo Station, Antarctica on a C-130 Hercules for the South Pole Station.

2.3 Muon rate measurement while flying to the South Pole

In December 2018, I flew to the South Pole as part of a field team to perform maintenance and upgrades on the IceCube Neutrino Observatory [10]. During the flight, I measured the ionizing radiation with two detectors oriented in configuration (d) of Fig. ???. Data was recorded to the microSD cards and powered through a single 30,000 mAh power bank.

The first four flights (from Madison, WI USA to Christchurch, New Zealand) were operated by United Airlines and New Zealand Airlines. The altitude data was publicly available for these flights on FlightAware.com [11]. The flight leaving from Christchurch New Zealand, to McMurdo Antarctica, was on a C-17 military jet operated by the US Air Force. Similarly, we flew on a C-130 Hercules, the day after to the South Pole. Since these were military flights, the altitude of this flight was not available; however, several altitude measurements on the second flight were made using GPS. We landed several days later on the 2820 m thick South Pole glacier, approximately 0.5 km from the actual Geographical South Pole.

The full master and coincident detector data are shown in Fig. 2.6, with descriptions of each flight in the text boxes. To give perspective for other measurements, the total data collected by the master detector was about 50 Mb, whereas the coincidence detector was approximately 15 Mb.

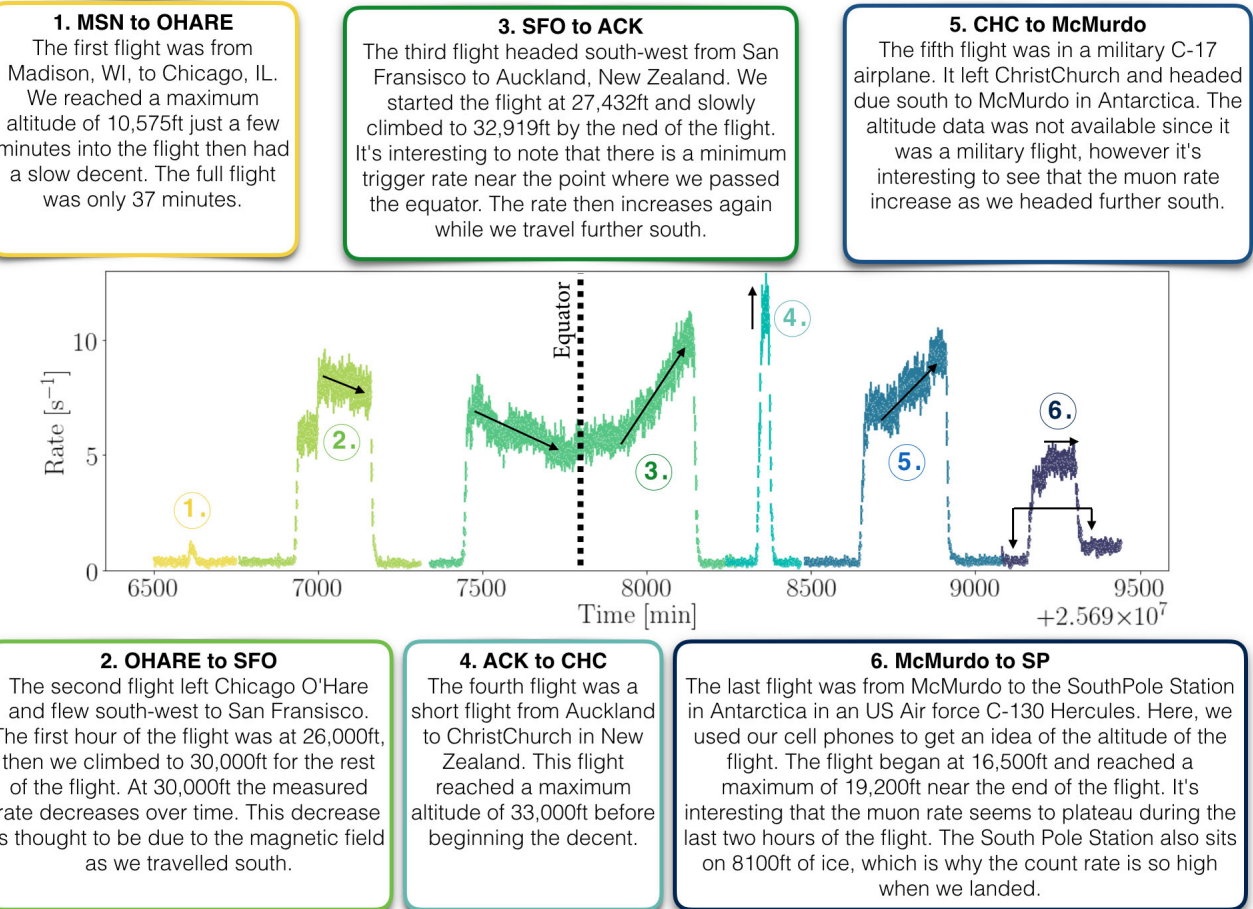


Figure 2.6

Fig. 2.6 illustrates several very interesting properties. First, there is a trend towards lower count rates near the equator. This is due to the latitudinal variation in the cosmic-ray flux described in Sec. ???. This effect is most obvious in the flight from SFO to ACK (labeled as flight 3 in Fig. 2.6), which traveled at nearly a constant altitude and a constant rate of latitude change from $+32^\circ$ to -32° . We see that the rate is not symmetric. This is because the magnetic latitude is offset from the geographical latitude, which in turn is because the magnetic field is not symmetric about the equator. Second, it's interesting to see that when we landed at the South Pole, there is a noticeable change in trigger rate due to the combination of the elevation and change in Earth's magnetic field.

While flying through the equator at 35,000 ft, I also performed an East-West measurement using configuration (e) of Fig. ???. We measure a count rate coming from the east of 0.69 ± 0.02 cps, while from the west 0.84 ± 0.03 cps. This represents a $22.2 \pm 7.4\%$ increase in the westward direction. This is due to the east-west asymmetry described in Sec. ???

2.4 Latitude correction to the cosmic-ray muons

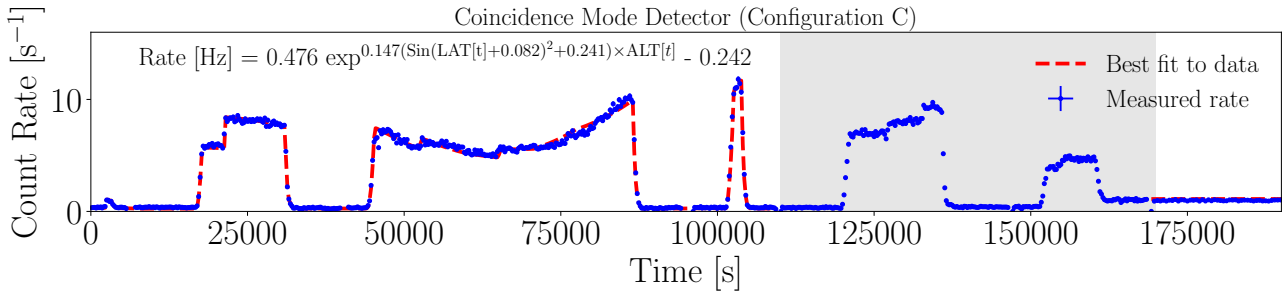


Figure 2.7: The fitted data based on the altitude and latitude data from the first four flights. The fit also includes a measurement after landing at the South Pole, where the altitude and latitude were known (2700 m and -90°). The two military flights were not included in the fit.

We observed latitudinal variation in the cosmic-ray muon rate in the previous measurements. This was an expected effect due to the change in the Earth's magnetic field as a function of latitude. Here, we will empirically attempt to account for the variation in the latitude and altitude based on the previous measurement. We will assume that the change in the rate as a function of latitude follows a sine-squared form, where the minimum occurs near the equator and the maximum occurs near the poles.

$$R[\text{Hz}] = N \exp^{\alpha(\sin(\text{LAT}[t]+\theta)^2+\beta) \times \text{ALT}[t]} - b \quad (2.3)$$

Here, θ represents a phase that offsets the latitude to account for the difference between the geographical latitude and the magnetic latitude, β is a factor that permits an altitude effect at the magnetic equator (set the sine term to zero), α is a scale factor that dictates the strength of the latitudinal and altitude effect, N is a normalization that sets the scale for the exponential component, and b is an offset that accounts for constant background radiation.

Fig. 2.7 uses the function in Eq. 2.3 to fit the data for the first four flights, plus the data after landing at the South Pole. The best fit values are shown at the top left of Fig. 2.7. Using this result, we can then invert Eq. 2.3 to calculate the altitude of the two military flights (assuming we flew at a constant velocity directly south). The calculated altitude is shown in Fig. 2.8 for the military flights in green, as well as the measured altitude from GPS in red.

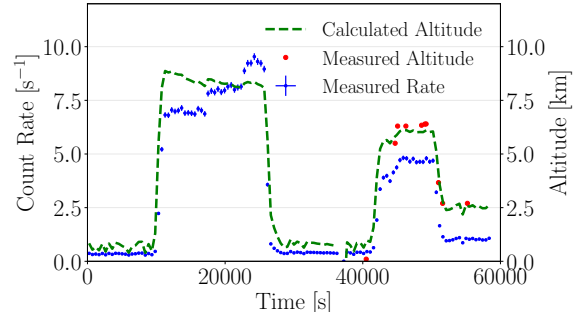


Figure 2.8: The measured muon rate in blue along with the calculated flight altitude in green. The red markers show the few GPS altitude measurements during the flight.

2.5 High-altitude balloon flight

Two detectors were flown in configuration (d) on a high altitude balloon (HAB) to map the ionizing radiation flux as a function of altitude. The balloon ascended to about 31 km deep, into the stratosphere, where primary cosmic rays begin interacting with atmospheric nuclei to produce extensive particle showers. Above roughly 5 km, the down-going ionizing flux of high energy (\gtrsim GeV) charged particles is dominated by protons [?].

The detectors were powered by a single 5,000 mAh battery pack, and data were recorded continuously to microSD cards. The onboard pressure measurements P is used to convert to geometric altitude h :

$$h = \frac{T_0}{L} \left[1 - \left(\frac{P}{P_0} \right)^{\frac{R L}{g M}} \right], \quad (2.4)$$

where $T_0 = 288.15$ K, $L = 0.0065$ K m^{-1} , $P_0 = 1013.25$ hPa, $R = 8.31$ $\text{J mol}^{-1} \text{K}^{-1}$, $g = 9.81$ m s^{-2} , and $M = 0.029$ kg mol^{-1} . Fig. 2.9 shows the event rate as a function of time (left axis), along with the calculated altitude on the right axis. The data exhibit the characteristic altitude profile: count rate increases with altitude, reaching a broad maximum near 20 km—the Regener–Pfotzer maximum [12], where secondary cosmic-ray production and attenuation balance. Above this altitude, the flux decreases as diminishing atmospheric depth reduces secondary particle production. At the peak count rate of 52 Hz the dead time remained below 2% of the livetime, indicating minimal accidental coincidence pileup.

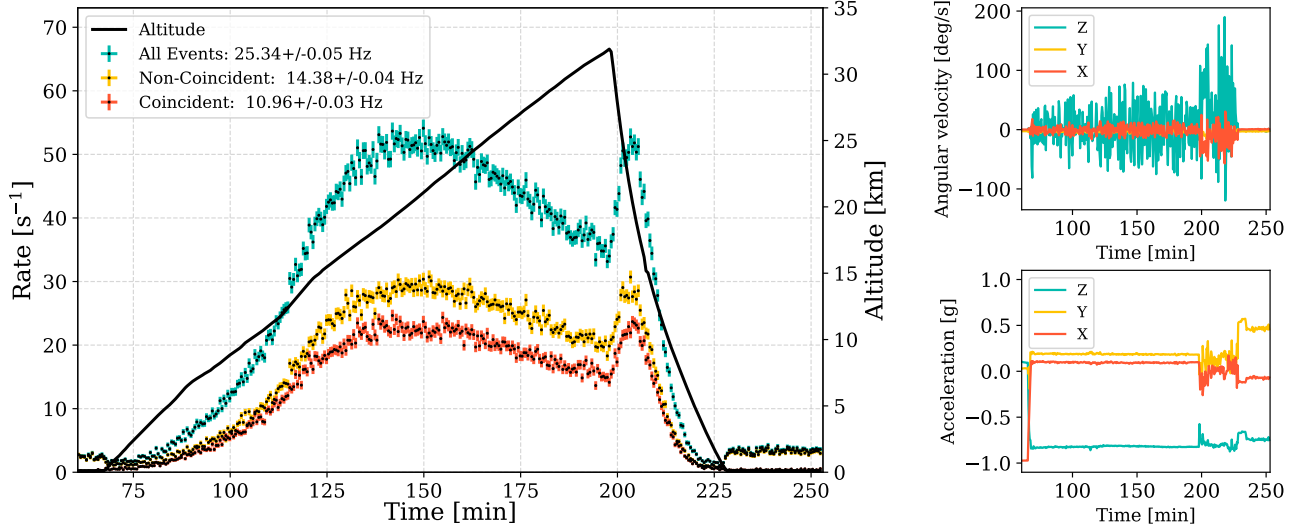


Figure 2.9: Left: The measured detection rate as a function of time during a HAB flight. The right axis shows the altitude calculated from the onboard pressure sensor. Right: The measured angular velocity (top) and linear acceleration (bottom) during the flight.

The built-in accelerometer indicated that the payload was initially oriented sideways during launch but realigned vertically shortly after liftoff (Fig 2.9 upper right), and the tether remained stable throughout the flight. The gyroscope revealed significant rotation about the

zenith throughout the flight (Fig 2.9 lower right). Temperature remained near 30°C in the troposphere and decreased to approximately 23°C at apogee in the stratosphere.

2.6 Cosmic-ray muon velocity

This measurement demonstrates the capability of BNC readout connected to the oscilloscope to perform time-of-flight (TOF) measurements to estimate the cosmic-ray muon velocities. Two detectors were vertically separated by $2.97 \text{ m} \pm 0.01 \text{ m}$, with their BNC outputs connected through equal length cables to a 50Ω -terminated, 200 MHz, 2.5 GSa/s Tektronix MDO34 oscilloscope. The oscilloscope was used to save the SiPM pulse waveforms directly to a computer when both channels crossed a 5 mV threshold. These waveforms were analyzed offline to extract precise pulse arrival times by fitting each waveform with a predefined pulse template. The time difference between pulses, Δt , was then used to calculate the muon velocity using the relation $v = d/\Delta t$, where d is the detector separation.

(Needs updates) The TOF measurement shown in Fig.2.10. Over the course of a week, 25 events were recorded which had a pulse separation below 10 ns. The resulting mean muon velocity (μ) and the standard deviation (σ) were determined by fitting a Gaussian to the distribution of the measured velocities. The results show a muon velocity of $0.92 \pm 0.09 c$, expressed as a fraction of speed of light.

(Plot x-axis should be "Velocity [v/c]") [done]

The accidental coincidence rate in the 10 ns timewindow, calculated using Eq. 2.2 is found to be 0.1 events per week.

To compare our measured velocity distribution with expectations from first principles, we performed a Monte Carlo simulation of the vertical muon flux at sea level using CORSIKA 7.7400 [?]. Primary cosmic rays were sampled from a Gaisser–Hillas spectrum of protons and helium nuclei between 10 GeV and 100 TeV, with the observation level set to 0 m a.s.l. and the US Standard Atmosphere profile. Secondary muons were filtered to include only downward-going tracks. The resulting muon energy spectrum dN/dE was binned logarithmically from 0.1 GeV to 1 TeV. To obtain the corresponding velocity spectrum, each energy bin center E_i was converted to a dimensionless speed $\beta_i = v_i/c$ via

$$\beta_i = \sqrt{1 - (m_\mu c^2/E_i)^2},$$

using $m_\mu c^2 = 105.66 \text{ MeV}$. The normalized binned counts $dN/d\beta$ were then compared to our time-of-flight measurement in Sec. 2.6.

The mean energy of the downgoign muons is 2GeV, which would have a velocity of 0.998c. I wonder if Agnieska or steph could give us a down-going muon energy spectrum, wich we could convert to a velocity spectrum and put in this curve.

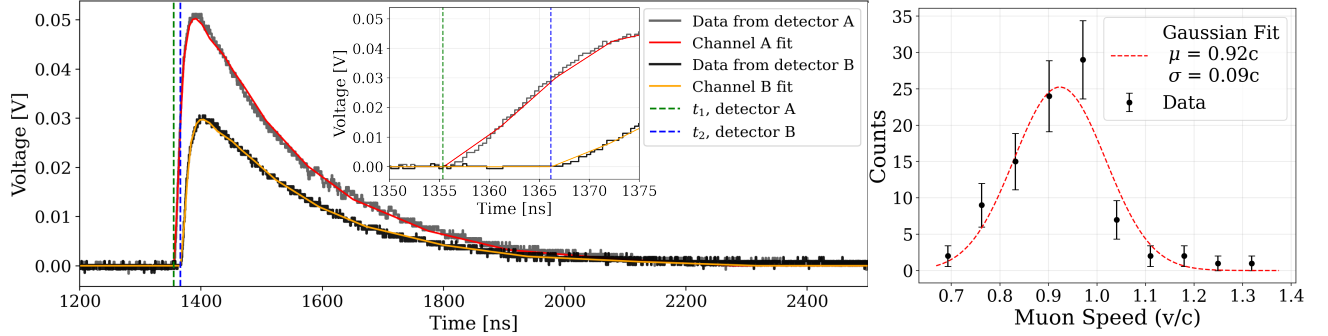


Figure 2.10: Left: An example waveforms and fitted pulses for top (red) and bottom (orange) detectors. Vertical dashed lines mark estimated muon arrival times. The inset image shows the rising edge of each pulse along with the fit. Right: The distribution of muon velocities, along with a fitted Gaussian in red.

2.7 Cosmic-ray muon attenuation in a Subway station

While visiting the Research Center for Neutrino Science (RCNS) at Tohoku University, we noticed that the Aobayama subway station was extremely deep underground and decided to investigate if there was a noticeable change in the muon rate compared to the office where we was working. After spending approximately 30 minutes in the station, we decided to travel to another station (Aoba-Dori Ichibancho station) a bit closer to my hotel to see if the rate changed, and then took a final measurement at ground level.

The muon attenuation was found to be surprisingly pronounced, as shown in Fig. 2.11. We would anticipate this measurement also working rather well in the deep subway stations. Are there any deep subway stations nearby? Washington Park station in Oregon is the deepest at 79m. Forest Glen station in DC is apparently pretty deep as well. If you measured the rate as a function of depth, you could reverse this, and use the detectors to tell you how far underground you are. This is a measurement of what we call overburden. It's often reported in meter-water-equivalent, which corresponds to the amount of water overhead that would be needed to have the same sheilding effect.

There are likely other underground areas in your area from which this measurement can be made. While the cosmic ray muon flux per unit solid angle is from directly above, the largest flux, per unit zenith angle, is actually near 70 degrees. To get a good measurement, you must not only consider the vertical overburden but also the overburden away from vertical.

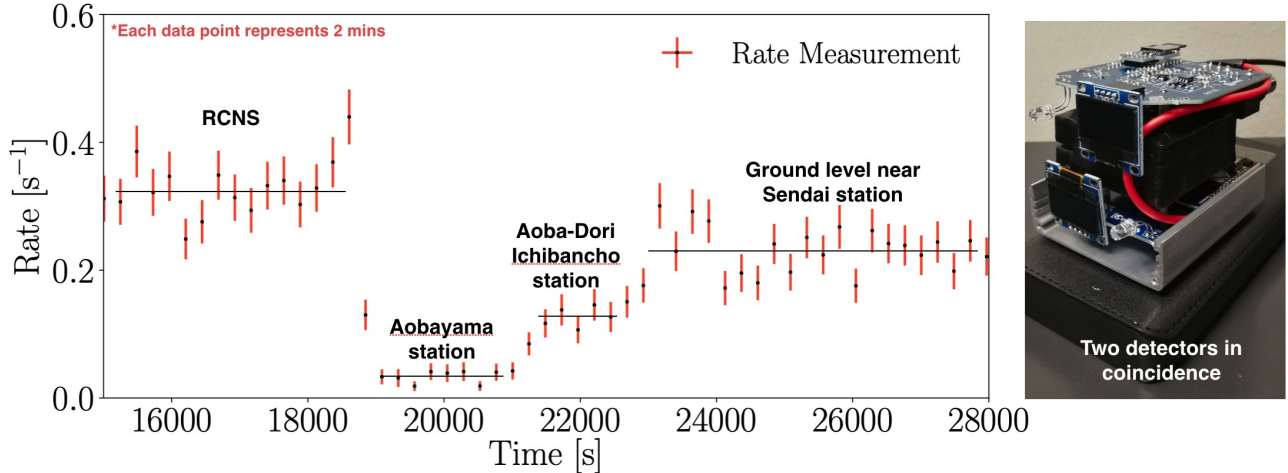


Figure 2.11: Subway in Japan.

2.8 Electromagnetic component of cosmic-ray showers

We've explored in Sec. ?? that at sea level, there exists a flux of electrons and positrons showering down on the Earth. The majority of this flux possesses energies less than 100 MeV, with a minimal contribution above 1 GeV. Subsequently, in Sec. ??, we delved into the fact that this electromagnetic component is not particularly penetrating and can be significantly attenuated with a few tens of centimeters of concrete (the radiation length in concrete, as found in Table ??, is 10.7 cm). To test this assertion, we can measure the coincidence rate on top of a building and then again several floors lower.

We anticipate minimal attenuation of cosmic ray muons, but a significant reduction in the electromagnetic component. A typical building often features around 15 cm of concrete between each floor. By measuring the vertical muon rate on the top floor and then repeating the measurement 5 floors lower, we expect the electromagnetic component's energy to be attenuated by 7 radiation lengths (a factor of 1000).

Two detectors were placed in coincidence mode, one atop the other, following configuration (c) of Fig. ???. They were positioned on the rooftop of the 10-floor WiPAC building for a 24-hour period, enclosed in a plastic bag for weather protection. Subsequently, the same two detectors were relocated to the 5th floor, and the measurement was reiterated. The outcomes of this measurement are presented in Fig. 2.12.

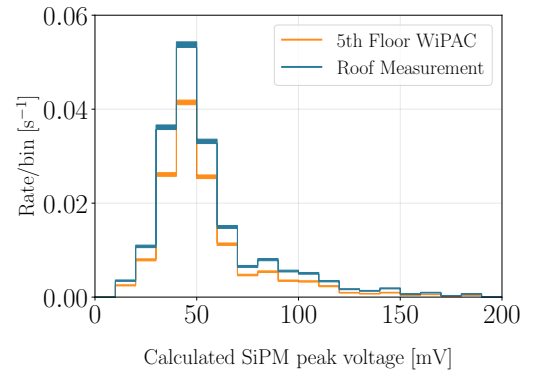


Figure 2.12: The calculated SiPM peak voltage on the roof of the WiPAC building compared to on the 5th floor.

The results reveal that the rate on the building’s top floor is 27% higher than the measurement made on the 5th floor. This discrepancy in rate is presumed to be primarily attributed to the reduction of the electromagnetic component. As elucidated in Sec. ??, we elucidate that approximately 33% of the total cosmic ionizing radiation flux at sea level emanates from the electromagnetic component.

We’ve always entertained the idea of conducting a study by submerging CosmicWatch into a lake. In such a scenario, the level of shielding is precisely defined and is commonly expressed in physics experiments in terms of meter water equivalent (m.w.e.). If you decide to embark on this experiment, ensure that your detectors are enclosed in a water-tight container. An anticipated 30% reduction in the coincident rate is expected within the initial few feet as the electromagnetic component diminishes. Following that, there will be a more gradual decline in the muonic component as you proceed deeper into the water, ideally reaching depths of tens of meters.

2.9 Reducing radioactive backgrounds

There is a notable presence of natural radioactivity in the environment that the CosmicWatch detector can detect. Certain items, such as orange FiestaWare plates from 1936-1943 used natural uranium for coloring, exhibit radioactivity (Prof. Axani has a few if you are interested in seeing them). Even common household items like potassium chloride (salt substitute) can produce a signal (requiring approximately 11 oz for detection). Additionally, granite countertops in homes might also exhibit radioactivity, so it's worth checking for.

Shielding against natural radioactivity in the environment can be challenging. Typically, at sea level, the largest component of our signal originates from radioactive backgrounds. Therefore, it is beneficial to explore ways to minimize this background and enhance the purity of the cosmic-ray muon signal (beyond using coincidence mode).

The use of dense materials around the detector can attenuate the incoming flux from background radiation. While an ideal choice would be a radio-pure material, we can illustrate the effect using lead bricks. Six lead ingots (each measuring $2'' \times 4'' \times 8''$) were strategically placed to provide 4π coverage around a single detector. The detector recorded data directly to the microSD card over the course of a full day. Subsequently, it was positioned on a workbench in the same room (far away from the lead) to measure the background spectrum for another full day. The resulting calculated SiPM peak voltage for the two measurements is depicted in Fig. 2.13. As anticipated, this setup significantly reduces events contributing to the low SiPM peak voltage region, which is predominantly influenced by radioactive background.

Lab 303 (AxLab) has several led bricks if you would like to use them. Alternatively, you can experiment with different materials, bury the detectors in the ground, or try using water (ensuring the detectors are sealed securely). Explore measuring the effectiveness of various materials of the same thickness and consider why some materials are more effective than others. Additionally, investigate the impact of different thicknesses of shielding.

Another experiment you can conduct involves studying the reduction in rate with distance from a radioactive gamma-ray source. To set up this experiment, you can contact a lab instructors, who have access to radioactive button sources located in Sharp Lab 016A. This experiment provides an opportunity to demonstrate the inverse square law ($1/r^2$) decay associated with ALARA (As Low As Reasonably Achievable) principles, a concept emphasized in radiation safety lectures.

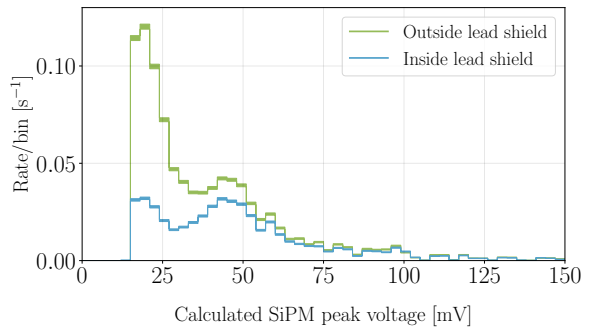


Figure 2.13: The effect of surrounding a single detector in a lead enclosure.

2.10 Correlation between the cosmic-ray muon rate and atmospheric pressure

A correlation exists between the atmospheric pressure and the cosmic-ray muon rate. It can be expressed as follows:

$$\frac{\Delta I}{\bar{I}} = \beta \Delta P, \quad (2.5)$$

where I represents cosmic-ray muon intensity, ΔP is the measured atmospheric pressure compared to the average pressure, and β is the barometric coefficient [13]. This correlation is actually the result of several processes outlined in Sec. ???. The barometric coefficient represents the percent change in detector count rate per hPa change in atmospheric pressure.

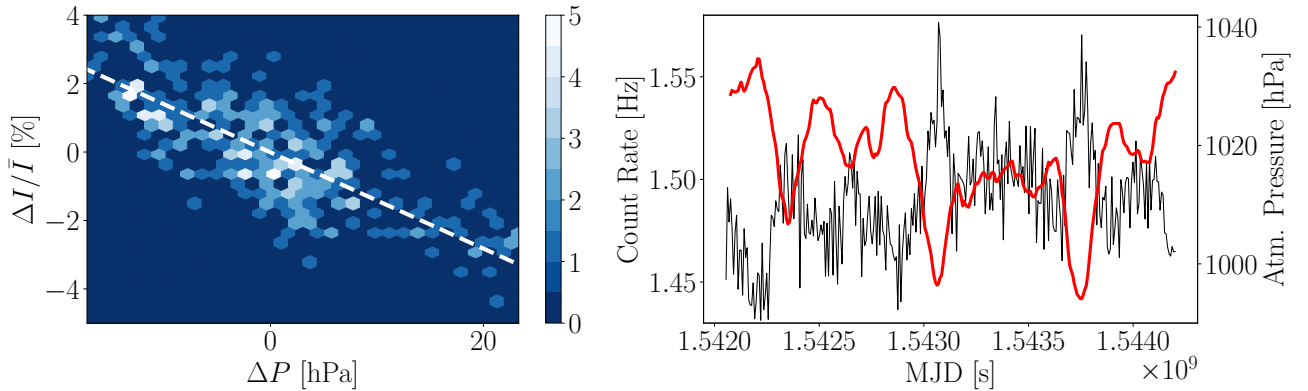


Figure 2.14: Left: The correlation between the atmospheric pressure and the detector count rate. Right: The detector count rate in blue and the atmospheric pressure in red as a function of modified Julian date (MJD). Both plots show the data binned with a bin size of two hours.

For this measurement, we decided to use an array of master-coincident detectors (ten detectors) to improve the statistics. Five pairs of detectors were each connected in configuration (c) of Fig. ???, and left to record the cosmic-ray muon rate over the course of 24.8 days (from 13:35 hrs Nov. 12th to 09:00 hrs Dec. 7th 2018.). Data was recorded directly to a microSD card and powered through an 8-way USB hub powered through a wall outlet. Since the CosmicWatch does not keep accurate time over long time-scales, we assume the time drifts linearly with time, and scale the uptime of all detectors such that they are all the same. This is not ideal, and we would recommend recording the data directly to a computer through the `import_data.py` script in the future to get an accurate time stamp on all events. However, this is more prone to losing data, since you would require a computer that runs continuously for a significant amount of time. The array of detectors was placed in the 4th floor WiPAC lab in Madison, WI. Atmospheric pressure for Madison was found in Ref. [14]. However, the UD version has a built in pressure sensor if you would like to try using it.

Fig. 2.14 (left) shows the correlation between the detector count rate and the atmospheric

pressure. The calculated correlation is shown in the dotted white line. A least squares fit yielded a barometric coefficient of $-0.141 \pm 0.007\text{ \%}/\text{hPa}$, in agreement with Ref. [15].

This may be difficult to do with only two detectors since the statistics will be lower, but it will be interesting to see! You can increase the amount of data you have if you ask a friend to also take data at their location, and you add that to yours.

One of our latest adventures is HurricaneWatch. A meteorology student who is a hurricane-chaser is taking our detectors into the storms she studies. The atmospheric pressure during a hurricane can drop by over 100 hPa, which we hope to be able to see. We will be excited to get this dataset!

2.11 A true random number generator?

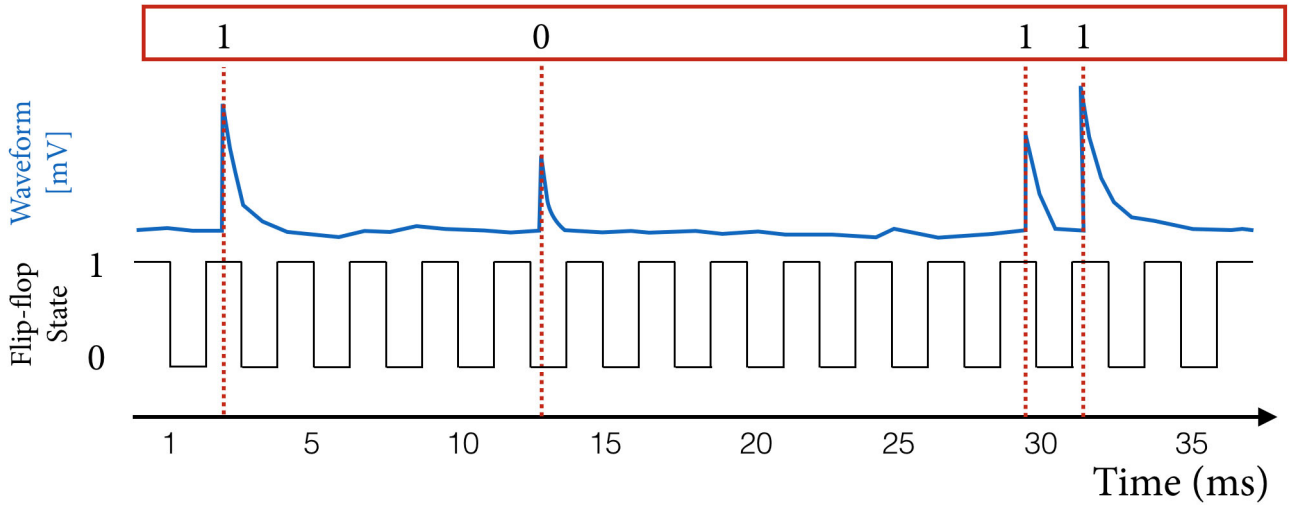


Figure 2.15: An illustrative diagram of the principle behind the random number generator. The x-axis indicates the time measure in milliseconds. Above this, we have the toggle flip-flop, which changes state every millisecond, then an illustrative waveform shown in blue. If the event triggered the detector while in the even state of the flip flop, we assign it a one, otherwise, we assign it a zero. This is shown in the red box at the top of the diagram.

Many applications require random numbers. Often, a random number may be generated through some algorithm, but this, therefore, becomes deterministic since if the user knew the algorithm and starting conditions, they could determine the output. An ideal random number generator would be derived from a truly random process, such as the arrival times of cosmic-ray muons or the radioactive decay of an element. The sum of two random processes will also be random, such as the signal from the radioactive backgrounds in the detector along with the cosmic-ray muon signal. For this measurement, we are following the description found in Ref. [8].

Any number can be expressed in terms of a sequence of ones and zeros; this is known as binary. An N -length sequence is able to represent a number from zero to $2^N - 1$ (corresponding to 2^N different values). For example, the 4-bit binary sequence "1011" corresponds to $1 \times (2^3) + 0 \times (2^2) + 1 \times (2^1) + 1 \times (2^0) = 8 + 0 + 2 + 1 = 11$.

We can convert the time stamp of a radioactive decay trigger into a "1" or a "0" using a *toggle flip-flop*. The toggle flip-flop is simply a state that changes from one to zero periodically (we will use a frequency of 1 kHz). If a particle passes through the scintillator during an even time stamp (as measured in milliseconds), we assign it a "1"; if it passes through an odd time stamp, we assign it a "0". After N triggers, we can build an N -bit random number. This is schematically illustrated in Fig. 2.15.

For this measurement, we use data taken from a 20-day background lab measurement. A single

detector was used. After triggering on a total of t events, we can build t/N N-bit random numbers. To illustrate this, if we choose to generate 8-bit random numbers (from 0 to 255), we can plot the number of each occurrence. This is shown in Fig. 2.16.

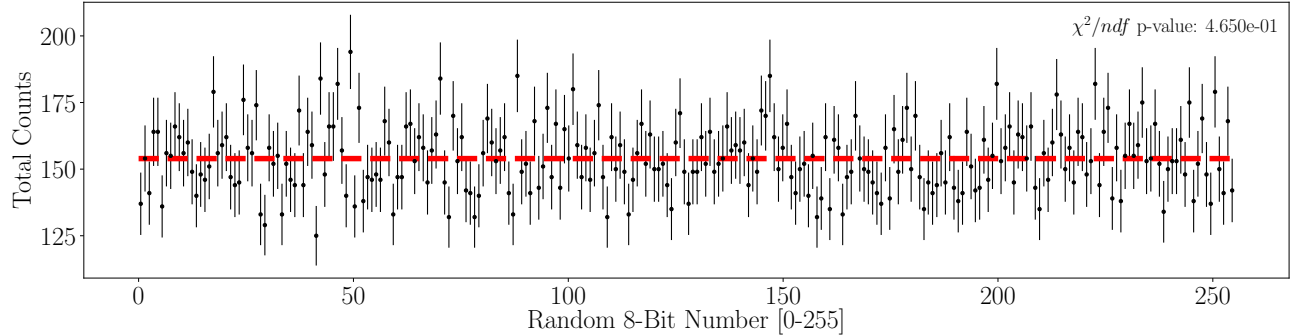


Figure 2.16: The number of occurrences of the generated numbers from 0-255. The reduced χ^2 p-value assuming that the distribution should be randomly distributed about the average number of occurrences is given at the top right of the figure.

Fig. 2.16 shows the random nature of the triggers. Each number should be equally probable to occur. The reduced χ^2 indicates a p-value for this assumption shown in the top right of the plot.

In your case, you may consider collecting data from a natural radioactive source. A suitable option is to acquire an 11 oz or larger container of salt substitute (potassium chloride) for this study. The radioactive emissions from the potassium chloride will contribute to a count rate that is higher than the background when the source is placed near the detector.

There are several factors that can introduce bias into the random number generator. Let's consider extreme scenarios. Imagine a scenario where the trigger rate is approximately 1 Hz, and the flip-flop state changes only every 10 seconds. In this case, the first ten triggers would yield all ones, followed by the next ten triggers giving all zeroes. This would result in biased high values for the initial numbers and biased low values for the subsequent ones. This example highlights the need for the toggle flip-flop to change states at a much higher rate than the trigger rate.

Another potential source of bias arises if the microcontroller fails to produce an equal number of even and odd timestamps due to



Figure 2.17: Background rate measurement with (left) and without (right) an 11 oz container of potassium chloride. The rates are measured as 7.2 ± 0.1 Hz and 3.94 ± 0.08 Hz, respectively.

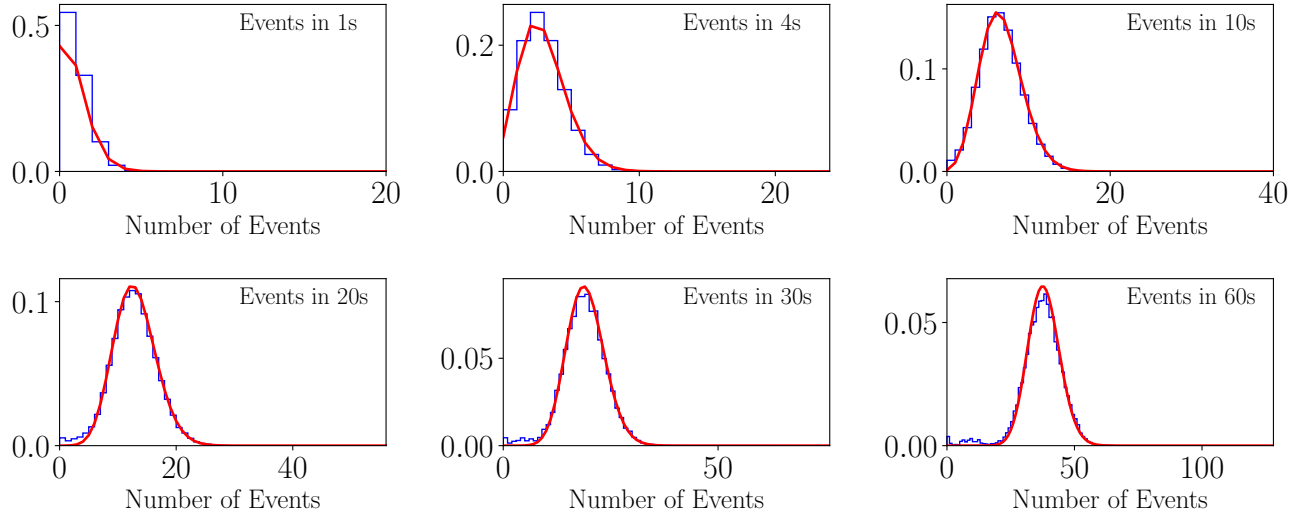


Figure 2.18: The distribution of number of events per unit time. Each cell represents a different amount of time in which the data is binned (labelled on the top right of each cell). The red line is the expected Poissonian distribution from Eq. ??.

internal configuration issues. For instance, when using the `microseconds()` function in Teensy/Arduino, the reported timestamp may only be accurate to the nearest even microsecond. It is crucial to thoroughly study and quantify the randomness of the data collected.

A funny thought could be to use this idea to turn the detector into a *magic eight ball*.

2.12 Gamma-ray spectroscopy

The detection material is primarily composed of polystyrene, a low-density synthetic hydrocarbon. Referring to Fig. ??, we observe that for carbon-based materials, at MeV gamma ray energies, the predominant interaction is Compton scattering. Ideally, in gamma ray spectroscopy, capturing the full energy of the gamma ray, as in photoelectric absorption (more common in high-density materials like germanium), is desired. However, in our case, a common interaction involves the original gamma ray undergoing Compton scattering within the scintillator, depositing some energy, and then leaving the scintillator. This results in a smeared energy distribution, lower mono-energetic peaks, and an increased rate in the Compton valley.

While challenging, some information can still be extracted from gamma ray sources, as exemplified in Fig. 2.19. In this context, data was collected with various sources at the MIT Junior Lab. Although we may not be able to discern monoenergetic peaks, interesting features emerge. For instance, Cobalt-60 emits two relatively high-energy gamma rays (1.17 and 1.33 MeV) compared to Cesium-137, which features a dominant gamma ray at 0.66 MeV. It is worth noting that the SiPM peak voltages, serving as a proxy for the number of observed photons and related to the energy deposited by a gamma ray, exhibit variations.

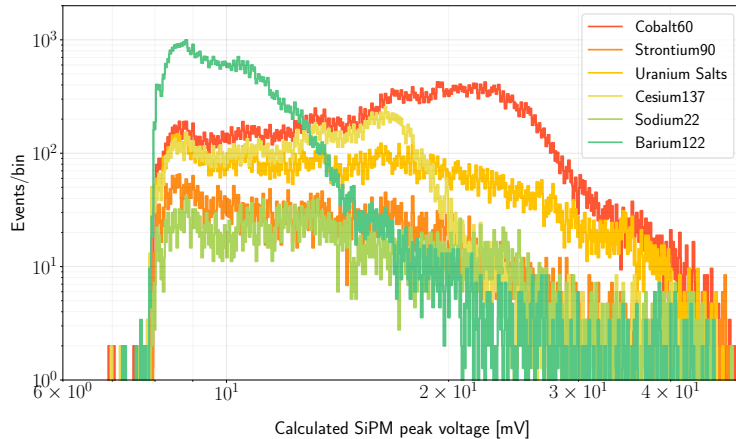


Figure 2.19: The distribution of number of events per unit time. Each cell represents a different amount of time in which the data is binned (labelled on the top right of each cell). The red line is the expected Poissonian distribution from Eq. ??.

Gamma ray spectroscopy with these detectors would be enhanced by utilizing a denser material, larger volume detectors, and greater photocathode coverage. We do have dense scintillator crystals if you would like to try.

2.13 Measuring the cosmic-ray muon rate in an airplane at 33,000 ft

A rate measurement was conducted during a flight from Boston International Logan Airport (BOS, latitude = 42.4°) to Chicago O'Hare Airport (ORD, latitude = 42.0°) using a single detector. The data was recorded onto a microSD card and powered by a 10,000 mAh USB power bank. The altitude of the airplane was obtained from flight records available on FlightAware.com [11].

Fig. 2.20 (left) illustrates the detector's trigger rate in blue as a function of time, binned into 60-second intervals. The error bars depicted are solely statistical. Airplane altitude data were linearly interpolated between points to estimate the altitude at any given minute. The interpolated altitude data were fitted to the detector data using a simple exponential plus an offset. Since the absolute take-off time was unknown (data recorded to the microSD card), we allowed the altitude timestamps to shift during minimization. The best-fit equation is displayed at the top left of this figure, where $\text{ALT}[t]$ represents altitude measured in kilometers as a function of time. The best-fit is also presented as a dashed red line.

Fig. 2.20 (right) displays the measured trigger rate as a function of true altitude. Here, we extend the exponential fit beyond the measured values. The count rate uncertainties were calculated by taking the square root of the sum of all events measured at a particular altitude. It's important to note that this data was collected with a detector in master mode, making it sensitive to background radiation from the interior of the plane.

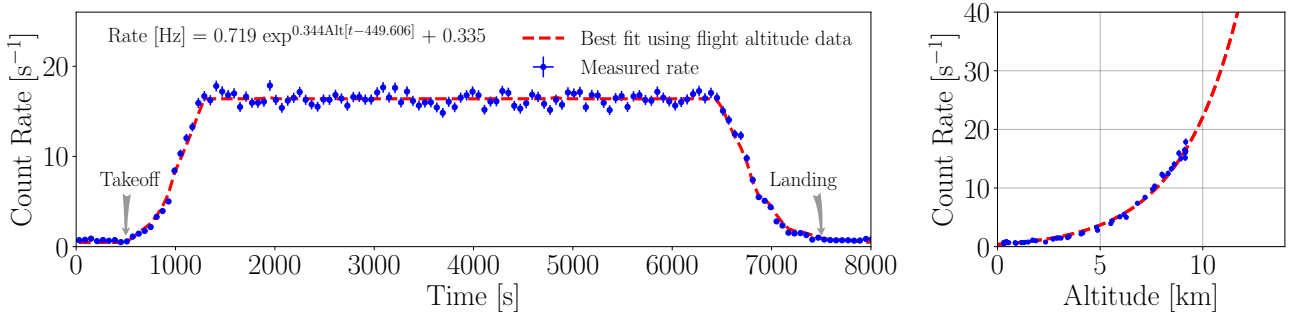


Figure 2.20: (Left) The count rate measured during a flight from Boston to Chicago as a function of flight time. The dashed red line shows the actual amplitude of the airplane [11] scaled by a fitted exponential shown at the top left of the plot. (Right) The measured count rate as a function of altitude. The dashed red line shows the fit.

The cosmic-ray muon flux is recognized to vary with latitude, a variation we have sidestepped by measuring the flux at a nearly constant latitude. Additionally, we anticipate the exponential fit to become less reliable as we extend to higher altitudes, owing to the alteration in flux composition near the primary cosmic ray interaction region.

2.14 High altitude balloon measurement at 107,000 ft



Figure 2.21: An image from the high-altitude balloon flight at 107,000 ft. Photo from *Daniel Kaczmar - DNF Systems*.

As mentioned in Sec. ??, primary cosmic rays interacting in the upper atmosphere produce showers of particles, some of which decay to muons. Muons are typically produced near an altitude of 15 km. At higher altitudes, there is an increase in the contribution from other ionizing particles, primarily from electrons/positrons and protons.

During the NearSpace2018 conference [16] in Torun, Poland, we participated in a high-altitude balloon (HAB) flight to measure the ionizing radiation flux as a function of altitude. Two detectors were used for the flight, allowing measurement of both the total rate on the master detector and the down-going rate on the coincident detector. The detectors were placed one-on-top of another (configuration (d) in Fig. ??) and taped together to ensure their orientation relative to each other remained constant throughout the flight. The BNC connectors and the OLED screens were removed from the PCB to reduce weight. An 8" 3.5 mm audio cable was used to connect them into coincidence mode, and the SDCard.ino code was uploaded to both detectors. An image of the two detectors is shown in Fig. 2.22. Both detectors were powered by a single-cell lithium-ion battery.

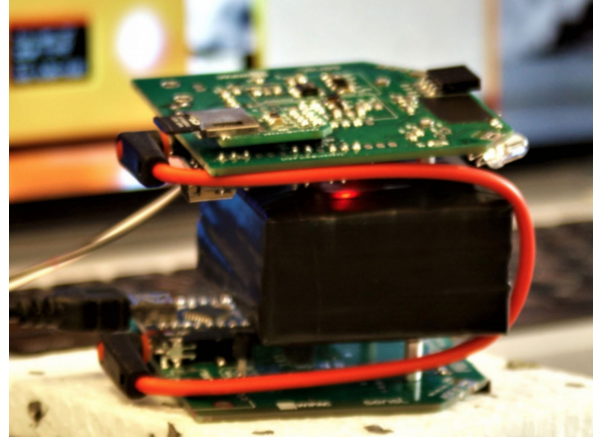


Figure 2.22: The two detectors flown in the HAB flight. The scintillators were taped together in order to preserve the detector orientation relative to each other.

The temperature during the ascent was expected to reach -60°C , requiring thermal protection for both the battery and to minimize the effect on the SiPM described in Sec. ???. A $10 \times 10 \times 10$ cm 3 Styrofoam enclosure with a wall thickness of 1 cm was constructed to house the components. It was large enough to accommodate the two detectors, a small heating element, and two single-cell lithium-ion batteries (one to power the detectors and the other to power the heater). A micro-switch was connected to the battery and wired outside the enclosure so that we could initialize the detectors from outside the enclosure just before the flight.

The HAB was launched on September 22nd, 2018, at 12:53 pm. DFN System recorded the balloon altitude and location using on-board GPS, and they mounted a camera to the balloon that looked down at the payloads. An image near the maximum altitude of the flight is shown in Fig. 2.21. The master (orange) and coincident (green) detector count rate, binned into 60-second intervals, is shown in Fig. 2.23, along with the altitude data from the GPS (black).

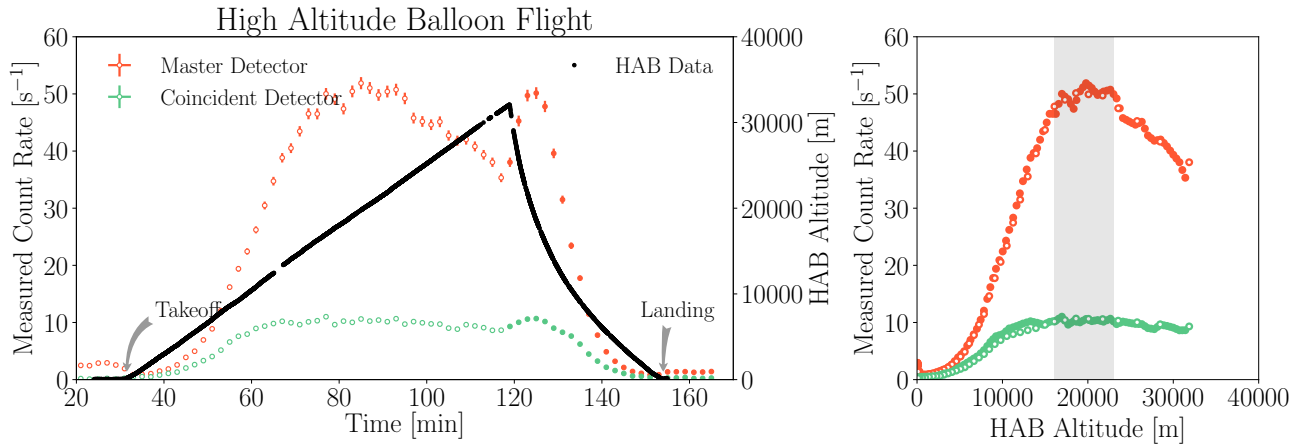


Figure 2.23: (Left) The measured trigger rate for the master (orange) and coincident (green) detector during the high-altitude balloon flight. Take-off occurred 30 minutes after powering on the detectors. The black data points correspond to the altitude as measured through the on-board GPS. (Right) The GPS altitude as a function of trigger rate. The uncertainty in both these plots are statistical.

The shape of the measured spectrum in Fig. 2.23 corresponds to the Pfotzer curve. We find an initial maximum count rate (Regener-Pfotzer maximum) for the master detector at an altitude from approximately 16-23 km, around 70-95 minutes into the measurement. After the balloon popped (at minute 118), the detectors fell through the Regener-Pfotzer maximum. The decrease in the trigger rate after passing the maximum occurs due to the detectors ascending beyond the primary interaction region.

The coincidence detector shows a flatter maximum at an altitude from approximately 12-25 km. The peak begins at lower altitudes since we are now preferentially triggering on vertically down-going particles. As described in Sec. ??, primary particles entering the Earth's atmosphere at larger angles from the zenith will interact at higher altitudes. In agreement with the data.

2.15 Rate measurement 1 km underground at Super-Kamiokande



Figure 2.24: Dr. Katarzyna Frankiewicz floating in the inner detector of Super-Kamiokande during the Gadolinium upgrade 2018.

Two Desktop Muon Detectors were brought to the Kamioka Observatory located 1 km underground in the Mozumi Mine, Japan. This mine is home to several high profile experiments, perhaps most notably the 2015 Nobel prize winning particle physics experiment, Super-Kamiokande. Two detectors were placed in the Super-Kamiokande control room for 8 hours, and connected together via a 6-inch 3.5 mm audio cable in configuration (c) of Fig. ???. The data was recorded from the coincidence detector through the `import_data.py` script directly to a laptop. Using the same detectors and set-up, a rate measurement was also performed outside the Kamioka mine in the observatory dormitory and in the airplane at 36,000 ft when travelling between Warsaw to Tokyo. Fig. 2.25 shows the trigger rate of the coincident detector for these three measurements, as a function of calculated SiPM peak voltage.

The total number of measured coincident events inside the Super-Kamiokande control room was found to be 101. It was observed that 96% of these events were located below the 50 mV peak described in Sec. ??, indicating that these are likely not minimum ionizing cosmic-ray muons.

The average rock density in the mine was measured to be 2.7 g/cm^3 , corresponding to approximately 2,700 m.w.e. (meter-water equivalent) of overburden [18]. Based on this, we expect the cosmic-ray muon rate to be attenuated by a factor of 10^5 compared to a ground-level measurement. With this assumption, we only expect approximately 0.04 cosmic-ray muon events over the 8-hour measurement in the Super-Kamiokande control room.

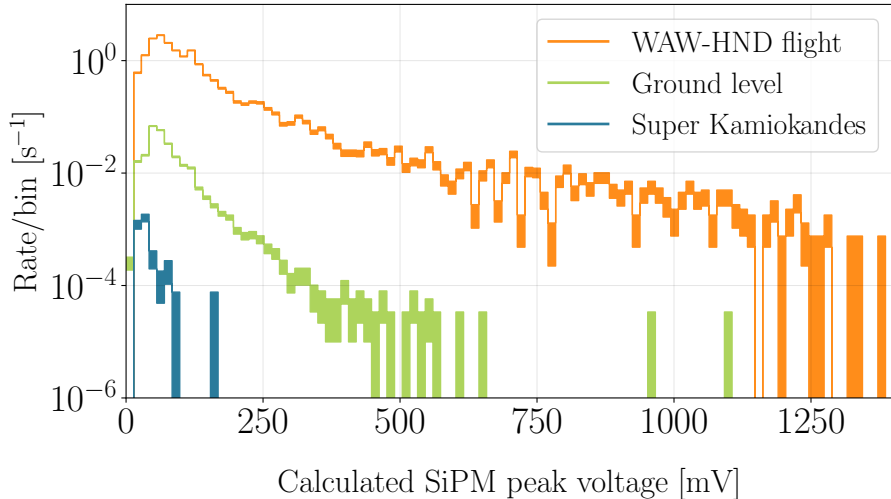


Figure 2.25: The measured coincidence rate at three locations. Data from Ref. [17].

The master detector count rate did not significantly change when it was brought into the mine, indicating that the radioactive background was still present in the control room. Given that the master detector count rate was 1 Hz, Eq. ?? suggests that we should expect 1-2 accidental coincidence events over the 8-hour period (see Sec. 2).

One unaccounted background (briefly mentioned in Sec. ??) consists of events in which a gamma-ray from a radioactive decay Compton scattered off the scintillator of the master detector, and then deposited sufficient energy in the coincident detector scintillator. This is thought to be the dominant source of triggers in this dataset, and a Monte Carlo simulation is currently being developed to investigate this. If these events originate from Compton scattering, we can estimate the rate for these types of events. Given the 101 events (with 1-2 assumed to be accidental coincidences and cosmic-ray muons), the calculated accidental Compton scattering coincidence rate in configuration (c) from Fig. ?? is found to be 0.0038 ± 0.0004 . A second 8-hour run was performed using the same configuration and location, which found 92 events (with a similar SiPM peak voltage spectrum) corresponding to a count rate of 0.0035 ± 0.0004 .

This result could be further investigated by repeating the measurement, this time with a thin piece of lead between the scintillators. Lead, being a dense material, is likely to either absorb the gamma-ray or absorb some of the energy from the gamma-ray through Compton scattering. Both processes would reduce the probability of measuring the event with the coincident detector. Another potential source for these events is correlated noise. If the lead does not alter the coincident count rate, this is a potential source for this signal; however, thus far, we have not found any evidence of events due to noise.

2.16 Portable trigger system for an accelerator beamline

This measurement was previously described in Ref. [17] and represents a practical use for the Desktop Muon Detectors.

A single detector, powered by a 10,000 mAh USB power bank, was placed in the Fermilab M-Test facility to trigger on secondary particles (GeV-scale pions and electrons) from the Main Injector. The purpose of this was to trigger a downstream data acquisition system for another experiment. The BNC output at the back of the detector is the raw SiPM pulse, which has a rise time of a few nanoseconds and a decay time of roughly $0.5\ \mu\text{s}$. This signal is useful for experiments that want to use a scintillator but require tens of nanosecond timing. The BNC output was connected to an 80 ft BNC cable to a NIM (Nuclear Instrument Module) rack. The signal passed through a $\times 10$ amplifier and into a discriminator. If the amplified signal was above a certain value, a binary signal was sent to an AND gate, where it was compared against another scintillator paddle trigger that was located on the other side of the other experiment. If the AND condition was satisfied (i.e., the particle passed through both the scintillator paddle and the Desktop Muon Detector), a binary signal was sent to the data acquisition system that began the recording of data of the downstream experiment. Fig. 2.26 shows the trigger rate of the detector placed in the beamline as a function of time. The beam spills occur every minute for two seconds.

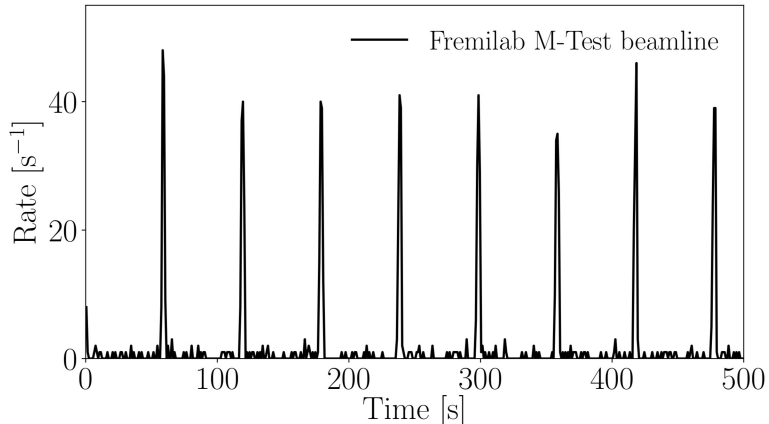


Figure 2.26: The trigger rate as a function of time of a single detector placed in the Fermilab M-Test beamline. Here, the detector is triggering primarily on GeV-scale pions and electrons from the Fermilab Main Injector.

The detector was identified as a useful beamline trigger due to its simplicity. This capability was facilitated by incorporating a BNC output directly connected to the SiPM. For this measurement, the approximate 10 ns uncertainty in the trigger was deemed acceptable. However, if users desire to utilize the FAST output of the SiPM for single nanosecond precision, the SiPM PCB could be modified. We plan on investigating this sometime in the future.

Chapter 3

UNTESTED MEASUREMENTS FOR THE ADVENTUROUS

This section outlines a selection of measurements that we aspire to include in the curriculum in the near future. Opting for one of these measurements means venturing into relatively unexplored territories. We highlight the challenges associated with these measurements, and in the case of the solar flare measurement, success depends on fortuitous timing! Therefore, exercise caution. Nonetheless, if you successfully conduct any of these measurements, they could potentially become part of next year's curriculum! Best of luck!

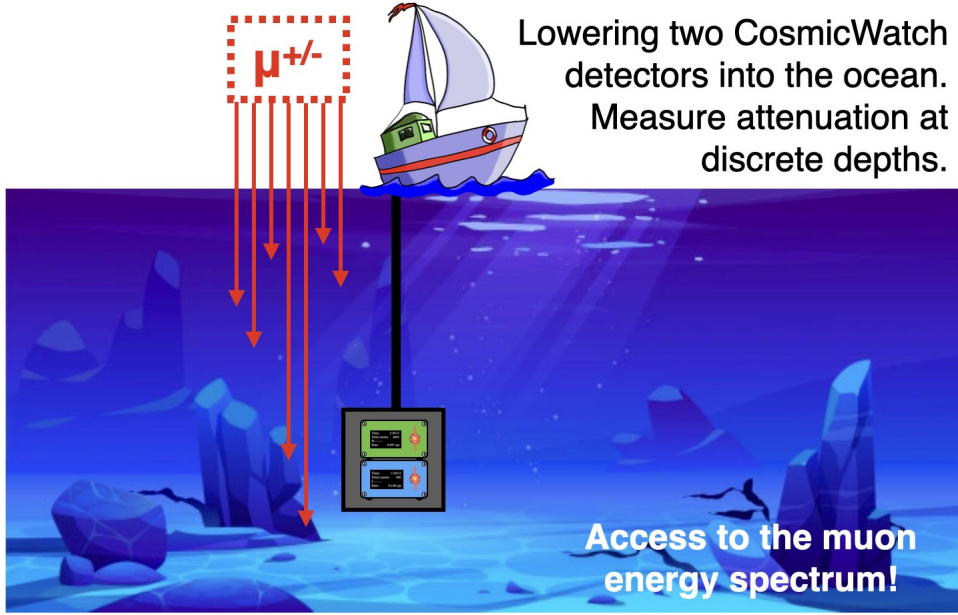


Figure 3.1: Measuring the muon rate as a function of depth underwater should be able to give you the muon rate.

3.1 Muon Rate Underwater

Physicists typically report the equivalent overburden in terms of how much water would provide the equivalent shielding. A measurement in actual water can be useful since it provides a homogeneous material and is abundant. We will attempt to measure the attenuation as a function of depth in a deep lake/ocean. Initially, we should observe a steep decrease due to the electromagnetic component dropping out, then a slow decrease as a function of depth. If you frequent a pool, they may let you take data in the deep end. A student at MIT dropped them in the Charles River to measure the attenuation.

It's neat actually. If you could measure how the rate decreases with depth, you should be able to extract the muon energy spectrum. That is, if muons had extremely high energies, they would penetrate deeper into the water. This would be a tricky bit of unfolding, but extremely cool.

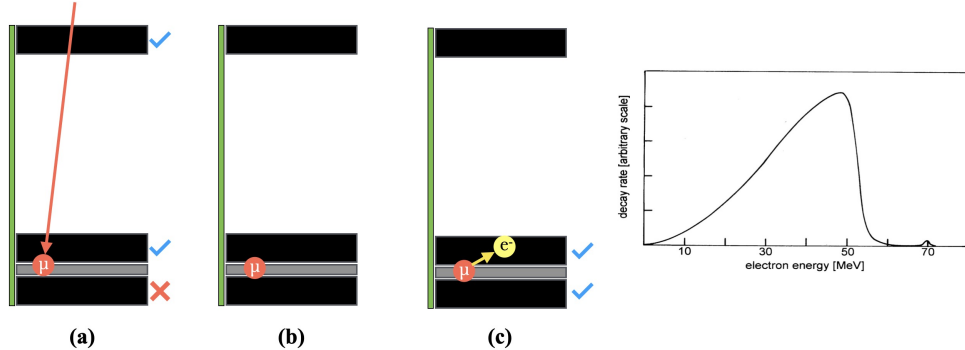


Figure 3.2: (a) A muon passes through the top and middle detector. (b) It hangs out for a bit. (c) the second or third detector observe something 100s of ns to a few microseconds later, as the muon decays to a Michel electron.

3.2 Muon lifetime

This is cool. It might be possible to measure the lifetime of the muon. As mentioned earlier in this document, the muon is unstable. Their rest mass is approximately $207 m_e$. It has a lifetime of roughly $2.2 \mu s$. The fact that muons are sufficiently energetic and decay only under the weak interactions causes that they can reach sea level. When it decays, it emits a two neutrinos (invisible to us), and a fairly energetic electron, called the Michel electron. The Michel electron energy spectrum is shown in Fig. 3.2 right. If you can stop a muon and see how long it hangs around for, you can get the muon lifetime. I think you will need three detectors though. We have a special detector in Lab 303 that might be suitable for this. It's shown in the image below, Fig. 3.2.

With three detectors one-on-top of each other, this measurement should be possible. The top two are used to trigger on an incoming muon. If the bottom detector doesn't trigger, that likely means that the muon stopped in the middle detector. Then you wait. Not long though, since after a few 100s of nanoseconds, the Michel electron should pop out and trigger either the middle or bottom detector. By measuring the time it takes between these two signals, you can infer the muon lifetime by fitting an exponential + constant to the Δt time between trigger and the Michel. The exponential decay constant represents the lifetime of the muon. The constant is there to account for the accidental coincidences, which are independent and therefore will have a constant rate.

3.3 Solar flares and the Forbush decrease

At higher altitudes and latitudes, where lower-energy primary cosmic ray particles are observable, a correlation between cosmic radiation and solar activity becomes apparent. Solar flares, often associated with coronal mass ejections, can lead to significant temporary increases in count rates. This effect is more pronounced at higher altitudes, where the Earth's magnetic field offers less protection to GeV cosmic ray particles compared to regions near the equator.

NASA and the National Oceanic and Atmospheric Administration operate the Geostationary Operational Environmental Satellite (GOES), which records the incident particle flux from the sun, including protons, electrons, and X-rays. Publicly available data from GOES can be used to correlate transient solar events with cosmic ray muons. Solar flares are classified using letters A, B, C, M, or X, representing the power per unit area of an event. A numerical suffix (0 to 9) indicates the event's strength; for example, an X2 flare has twice the strength of an X1 flare. Each letter classifies events with an order of magnitude difference between classes, with X denoting the most powerful flare classification. While X-class solar flares are relatively rare, occurring only a few times per year, there's a chance your detector might be active during such an event!

The real-time clock on CosmicWatch detectors is updated each time the software is re-uploaded to the Teensy 4.0. Over time, clock drift may occur, leading to an inaccurate local time stamp. However, this might not be a significant issue since solar flares can have relatively long durations. If clock drift is a concern, data can be recorded directly to the computer, where the computer's time stamp is replaced with the RTC time stamp, providing a more accurate reading.

Roughly one day after a solar eruption, the Earth undergoes a solar storm. A brief increase in the magnetic field is observed, followed by a much more pronounced decrease that persists for several hours. Over the span of a few days, the magnetic field gradually returns to its initial strength. This phenomenon is known as the "Forbush decrease." Initially, the observed cosmic ray radiation intensity starts to decrease.

Given the crucial role of Earth's magnetic field in shielding us from cosmic radiation, this effect should also be observable. As illustrated in Fig. 3.3, the change in rate is at the percent level. Changes at the percent level should be detectable over the course of a day using configuration (d) of Fig. ???. However, it's important to note that atmospheric conditions may also influence the measurement, so considering barometric pressure measurements could be beneficial.

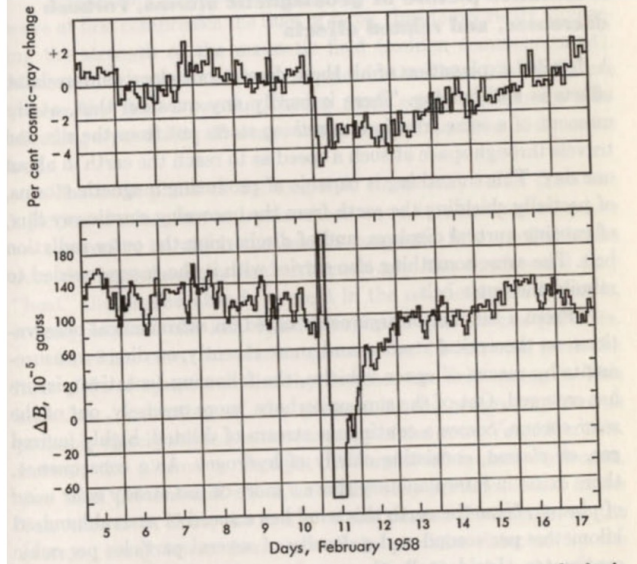


Fig. 14-2 Typical Forbush decrease. The lower curve represents the horizontal component ΔB of the magnetic field measured, from an arbitrary zero, in units of 10^{-6} gauss. The upper curve shows the corresponding variations of cosmic-ray intensity (measured by a neutron monitor in Chicago) as a percentage of the normal intensity. Shown on the horizontal axis is the universal time, in days. (From F. Bachelet, P. Balata, A. M. Conforto, and G. Marini, *Il Nuovo Cimento*, vol. 16, p. 292, 1960.)

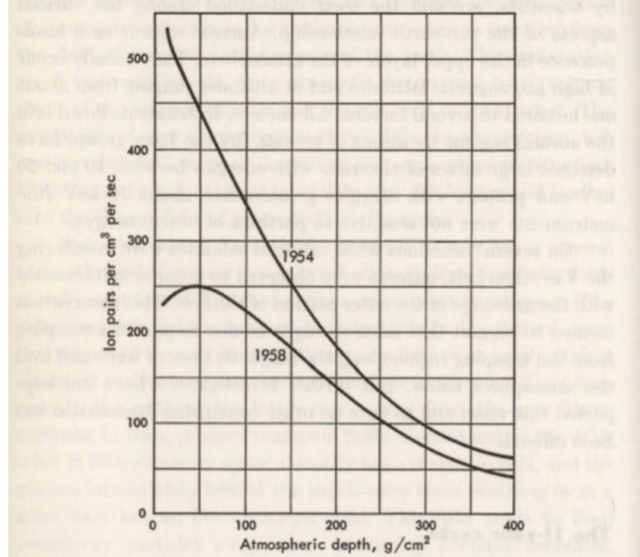


Fig. 14-3 Intensity of cosmic rays as a function of atmospheric depth, measured at a geomagnetic latitude of 88° N at the time of minimum solar activity in 1954 and at the time of maximum solar activity in 1958. The instrument used was an electroscope; the vertical scale gives the number of ion pairs per second produced by cosmic rays in 1 cm^3 of air at standard temperature and pressure. The horizontal scale gives the atmospheric depth, in grams per square centimeter. (From H. V. Neher, *Nature*, vol. 184, p. 423, 1959.)

Figure 3.3: The Forbush decrease (left) and solar maximum/minimum cosmic-ray flux (right). This figure comes from Ref. [3].

3.4 Measuring the air shower size

Air showers were first discovered using coincidence counters, a concept very similar to the one employed in CosmicWatch. An air shower involves multiple particles arriving simultaneously. Such showers can occur when muons interact while traversing material above the detector, such as the building's roof, or, as depicted in Fig. 3.4, a sheet of lead.

The objective of this measurement is to investigate coincident events between two sets of coincidence detectors based on the lateral distance between the two sets. The challenge lies in the potential requirement for 3 to 4 detectors, as illustrated in Fig. 3.4. Two sets of coincidence detectors (totaling 4 detectors) would yield a lower accidental coincidence rate compared to using 3 detectors (excluding detector C). While the detectors are not configured to record triple coincidences via the microSD card, connecting all detectors to a single computer (via a USB hub) allows the data from each detector to be saved in a unified file using the `import_data.py` script. The timestamps from the computer data can then be analyzed to identify coincidence events.

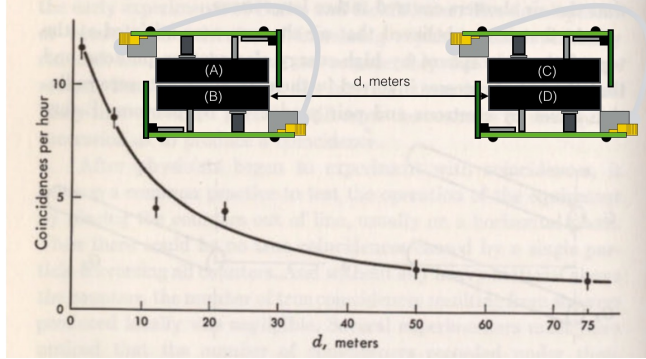


Figure 3.4: Recommended configuration for measuring air shower size. Data from Ref. [3].

This section compiles a list of potential future experiments that we intend to perform. After gather and analysing the data, these will be added into Sec. 2.

1. **cosmic-ray muon rate at different floors of a large concrete building:** Large concrete buildings, like FermiLab would be great to measure the floor to floor vertical attenuation.
2. **Special relativity measurement:** A repeat of the measurement that confirmed special relativity by measuring the muon rate on top and at the bottom of a mountain. This can be demonstrated using the altitude data here; however, climbing a mountain would make a good story.
3. **Thin lead measurements.** Thin lead sheets, above the coincidence detectors will actually cause an increase in the count rate. This is due to the muon creating a shower of secondaries, that spread out and are able to trigger the detectors simultaneously. After a few inches of lead, the shower is attenuated.
4. **Clean room background measurement.** Background measurement in clean room at SNO+, also a coincidence measurement.
5. **Measure the Southern Atlantic Anomaly.** This could be performed by flying from Mexico to northern Africa.
6. **Extreme weather events:** Measure muon rate during a low pressure event – like a hurricane.
7. **Solar flare events:** Capture data during an intense solar flare.
8. **Solar activity:** There is an 11-year due to the solar activity that modulates the low-energy cosmic rays.

Chapter 4

CONCLUSION

The CosmicWatch Desktop Muon Detectors offer a versatile platform for exploring diverse natural phenomena. This document provided a comprehensive overview of the underlying physical processes influencing the detectors and demonstrated how valuable insights can be derived from the collected data. The detectors can be employed to investigate a wide range of phenomena related to the geomagnetic field, atmospheric conditions, cosmic-ray shower composition, particle attenuation in matter, radioactivity, and statistical properties of Poisson processes. Students are encouraged to further develop the concepts introduced or design their experiments. Feedback is highly welcomed to enhance and refine this manual. Enjoy your exploration with the CosmicWatch detectors!

Bibliography

- [1] K. O. et al, “Cosmic rays - particle data group,” *Nuclear Instruments and Methods in Physics Research Section A: Accelerators, Spectrometers, Detectors and Associated Equipment*, vol. 38, no. 090001, p. 6, 2014.
- [2] S. K. LBNL, “32. passage of particles through matter,” 2017.
- [3] B. Rossi, “Cosmic rays,” 1964.
- [4] M. W. Friedlander, *A thin cosmic rain: Particles from outer space*. Harvard University Press, 2002.
- [5] P. K. Grieder, *Cosmic rays at Earth*. Elsevier, 2001.
- [6] T. K. Gaisser, R. Engel, and E. Resconi, *Cosmic rays and particle physics*. Cambridge University Press, 2016.
- [7] W. R. Leo, *Techniques for nuclear and particle physics experiments: a how-to approach*. Springer Science & Business Media, 2012.
- [8] C. Grupen and B. Shwartz, *Particle detectors*, vol. 26. Cambridge university press, 2008.
- [9] H. Kolanoski and N. Wermes, *Particle detectors: fundamentals and applications*. Oxford University Press, 2020.
- [10] K. Albrecht *et al.* (The IceCube Collaboration), “IceCube - the next generation neutrino telescope at the South Pole,” *Nuclear Physics B-Proceedings Supplements*, vol. 118, pp. 388–395, 2003.
- [11] Flight Aware. <https://flightaware.com/>, Dec. 2017.
- [12] E. Regener and G. Pfotzer, “Vertical intensity of cosmic rays by threefold coincidences in the stratosphere,” *Nature*, vol. 136, no. 3444, p. 718, 1935.
- [13] R. De Mendonca, J.-P. Raulin, E. Echer, V. Makhmutov, and G. Fernandez, “Analysis of atmospheric pressure and temperature effects on cosmic ray measurements,” *Journal of Geophysical Research: Space Physics*, vol. 118, no. 4, pp. 1403–1409, 2013.
- [14] LocalConditions.com. <https://www.localconditions.com/weather-madison-wisconsin/53701/past.php>, accessed: Dec. 2018.

- [15] K. Jourde, D. Gibert, J. Marteau, J. de Bremond d'Ars, S. Gardien, C. Girerd, and J.-C. Ianigro, "Monitoring temporal opacity fluctuations of large structures with muon radiography: a calibration experiment using a water tower," *Scientific reports*, vol. 6, p. 23054, 2016.
- [16] <http://nearspace.pl/>, "Near space conference 2018," Dec 2018.
- [17] S. N. Axani, K. Frankiewicz, and J. M. Conrad, "The cosmicwatch desktop muon detector: a self-contained, pocket sized particle detector," *Journal of Instrumentation*, vol. 13, no. 03, p. P03019, 2018.
- [18] M. Fukugita and T. Yanagida, *Physics of Neutrinos: and Application to Astrophysics*. Springer Science & Business Media, 2013.